ACS OMEGA

http://pubs.acs.org/journal/acsodf

Article

One-Step Pyrolysis Fabrication of Magnetic Bagasse Biochar Composites with Excellent Lead Adsorption Performance

Jinming Chang, Sheng Yu, Yunwen Liao, Xiaoyu Guan, Hejun Gao,* and Yulong Li

Cite This: *ACS Omega* 2022, 7, 42854−42864

Read Online

ACCESS | Metrics & More | Article Recommendations | Supporting Information

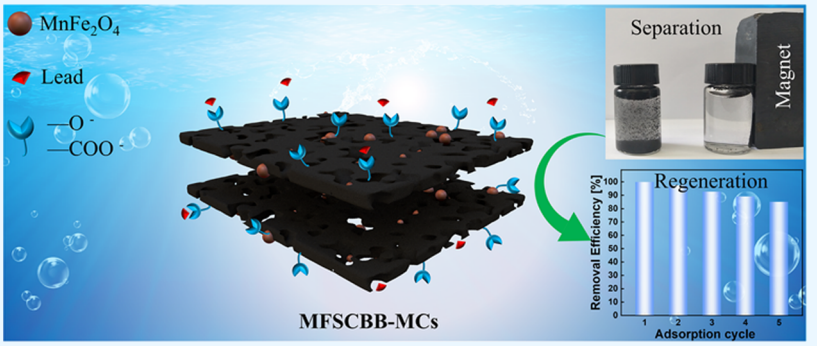

ABSTRACT: In the present study, a magnetically separable adsorbent, manganese ferrite ($MnFe_2O_4$)/sugarcane bagasse biochar magnetic composites (MFSCBB-MCs), was fabricated through a one-step pyrolysis method. The characterization of the prepared adsorbents indicated that $MnFe_2O_4$ nanoparticles were successfully embedded into the biochar matrix, offering magnetic separability and increasing the negative charges on the surface relative to the pristine biochar. Batch adsorption tests indicated that the adsorption of lead on MFSCBB-MCs was pH- and dose-dependent. The experimental results were effectively fitted using the pseudo-second-order kinetic model ($R^2 > 0.99$) and the Langmuir isotherm equation ($R^2 > 0.99$), indicating the main chemisorption pathway and monolayer coverage process. Meanwhile, lead adsorption was found to be spontaneous and endothermic, as shown by the study of thermodynamic parameters. The maximum capacity, q_m, calculated from the Langmuir model was 155.21 mg·g^{-1} at 25 °C, demonstrating excellent adsorption capability compared with several previously reported bagasse adsorbents. Based on adsorption mechanism analysis, physical adsorption, electrostatic attraction, and complexation were all involved in the lead(II) adsorption process on MFSCBB-MCs. Furthermore, the adsorbent was easily regenerated as indicated by the high magnetic separation and chemical desorption potential after five cycles, so it is a cost-effective and environmentally favorable adsorbent for wastewater lead removal.

1. INTRODUCTION

Heavy-metal-contaminated water derived from industrial effluents and municipal wastes, along with growing urbanization and industrialization, presents serious threats to public health and ecosystems.[1,2] Lead has been widely explored owing to its known toxic nature and constant bioaccumulation throughout the food web. The emission of lead in drinking water has been limited to less than 0.01 mg·L^{-1} through strict environmental safety regulations.[3] Studies should explore an effective approach to alleviating lead-associated water pollution.

Physical or chemical methods have been previously used for the removal of lead from water, such as adsorption, membrane separation, ion exchange, and chemical precipitation methods.[4] Adsorption is one of the most prospective alternatives owing to its flexibility, time-saving, convenient operation, and cost-effectiveness. Several adsorbents have been successfully developed and applied in the purification of lead-contaminated water, such as activated carbon,[5] zeolites,[6] activated alumina,[7] clay,[8] and sugarcane bagasse (SCB).[9,10] SCB is an economical and renewable biomaterial with abundant polar groups (carbonyl, carboxyl, and hydroxyl groups) and a strong coordinating affinity to heavy metals irons. However, raw SCB cannot be directly employed as an adsorbent due to its unstable structure, poor regeneration, low porosity, and limited metal adsorption capacity.[11,12] To address these limitations, raw SCB is modified and functionalized by loading additional polymers/inorganic material and carbonization to increase its applicability in environmental remediation including lead

Received: August 1, 2022
Accepted: October 28, 2022
Published: November 14, 2022

Scheme 1. Schematic Illustration of the Synthesis Procedure and Structure of MFSCBB-MCs (photograph courtesy of 'Sheng Yu'. Copyright 2022)

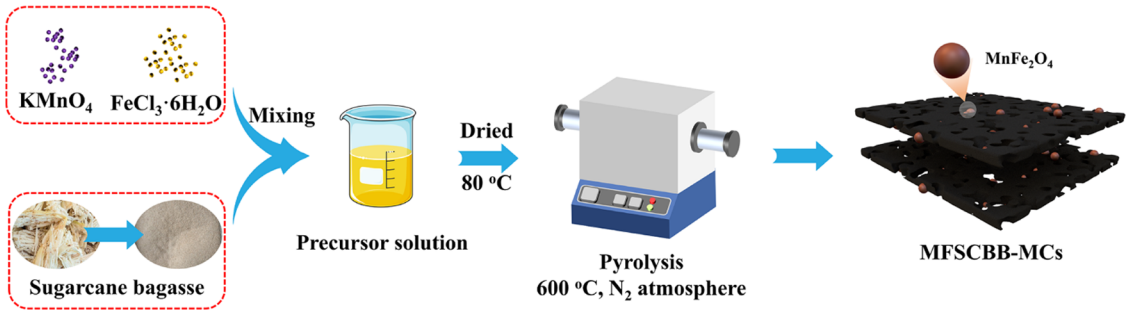

sorption. Currently, the most attractive technique for improving SCB is hydrothermal carbonization, which imparts a large specific surface area, microporous structure, and stable chemical characteristics to the resultant biochar, thus offering a higher adsorption capacity.[13,14] El-Banna et al. developed oxidized SCB biochar for lead sorption and reported that chemical oxidation improved the physicochemical properties of biochar.[15] Doumer et al. reported that SCB-derived biochar had a high sorption capacity for Cd(II), Cu(II), lead, and Zn(II), making it suitable for the treatment of heavy-metal-contaminated water.[16] The findings of these investigations typically demonstrated higher effectiveness of metal removal from aqueous solution. However, these SCB-produced biochar sorbents were difficult to separate and recycle. The residual sorbent species are potential secondary contamination risks. Therefore, SCB biochar sorbents with "recovery−reuse" capability for lead removal from water should be developed.

Limited studies report the fabrication and application of magnetic SCB biochar sorbents. Rattanachueskul et al. used Fe_3O_4/SCB biochar composites to remove undesirable tetracycline from water.[14] Dong et al. removed 17β-estradiol from an aqueous solution using magnetic SCB biochar nanoparticles.[17] Yi et al. prepared SCB magnetic biochar using steel pickling waste liquor, which was eventually used for Cr(VI) removal.[18] Notably, the approaches mainly magnetized the final SCB biochar by introducing iron oxides. In addition, most of the fabrication methods involve multistep and complicated procedures, such as initial co-precipitation, followed by pyrolysis. Moreover, the incorporation of common magnetite (Fe_3O_4) endows the biochar with magnetic separation ability; however, it does not always improve heavy metal removal efficiency.[19,20] Previous studies report that the predominant lead species in solution at a maximum pH of about 9.0 are Pb^{2+} and $[Pb(OH)]^+$. The zero-point charge (pH_{zpc}) of iron oxides is in the neutral pH range, implying that loading Fe_3O_4 increases the surface positive charge in an acidic environment, which can restrict adsorption to cationic lead species due to electrostatic repulsion.[21,22]

Manganese oxides are more suitable for adsorbent preparation compared with iron oxides, particularly for the elimination of cationic contaminants. Manganese oxides exhibit a porous structure, and their surface charge is generally negative throughout a wide pH range. As a result, several studies currently explore the incorporation of Mn into iron oxides to form manganese iron oxides ($MnFe_2O_4$). $MnFe_2O_4$ is insoluble in water and preserves its magnetic properties as well as the effective sites (carboxyl and hydroxyl groups) accessible for pollutant adsorption. Significant adsorptive removal of heavy metals (Ni, Hg, Cd, Zn, Pb, Cu, and Cr) and arsenic have been achieved with the aid of $MnFe_2O_4$ nanopowders or $MnFe_2O_4$-loaded composites.[23,24] These findings imply that loading $MnFe_2O_4$ onto the pristine SCB biochar can improve lead adsorption ability and promote effective separation through an external magnetic field.

Therefore, $MnFe_2O_4$/SCB biochar magnetic composite (MFSCBB-MCs) was prepared in the current study through a one-step pyrolysis method. The structure of MFSCBB-MCs, its potential for lead removal from solutions, and magnetic separation performance were systematically characterized and evaluated. A series of batch experiments with varied pH, adsorbent dose, contact time, initial lead concentration, and temperature were performed to explore the effects of operational parameters on the lead removal capability of MFSCBB-MCs. The adsorption mechanism was determined using X-ray photoelectron spectroscopy (XPS) and different mathematical models, for instance, kinetics, isotherms, and thermodynamics. Moreover, the feasibility of regenerating exhausted adsorbents through chemical desorption and their recyclability were explored. The findings of this study provide a recyclable adsorbent with enhanced lead remediation ability and effective magnetic separation property.

2. MATERIALS AND METHODS

The materials used in this study and characterization of MFSCBB-MCs are available in the Supporting Information.

2.1. Preparation of MFSCBB-MCs. MFSCBB-MCs were synthesized through a one-step pyrolysis procedure. SCB was cleaned by thoroughly washing it with distilled water to remove any adhering dust and sugar. The clean SBC was then dried for 48 h at 80 °C, pulverized, and finally sieved using a 200-mesh screen to obtain a powder of uniform size. One gram of SCB powder was homogeneously dispersed into a 100 mL solution containing 0.01 mol·L^{-1} $KMnO_4$ and 0.01 mol·L^{-1} $FeCl_3$ under ultrasonic oscillation. The mixture was heated in a beaker at 80 °C for 24 h to obtain a brown solid precursor. The precursor was pyrolyzed in a digital temperature control tube furnace (GSL-1500X, Hefei Kejing Material Technology Co., Ltd., China) at 600 °C for 1 h under a nitrogen atmosphere and a heating rate of 5 °C·min^{-1}. The residues obtained were cooled under a nitrogen atmosphere. The residues were severally washed with ultrapure water (18.2 MΩ·cm, 25 °C) and dried under a vacuum at 80 °C overnight to obtain MFSCBB-MCs. The synthesis process and structure of MFSCBB-MCs are presented in Scheme 1. Pristine SCB biochar (only pyrolyzed, donated as SCBB) was also prepared through the same procedure for comparison.

https://doi.org/10.1021/acsomega.2c04882
ACS Omega 2022, 7, 42854−42864

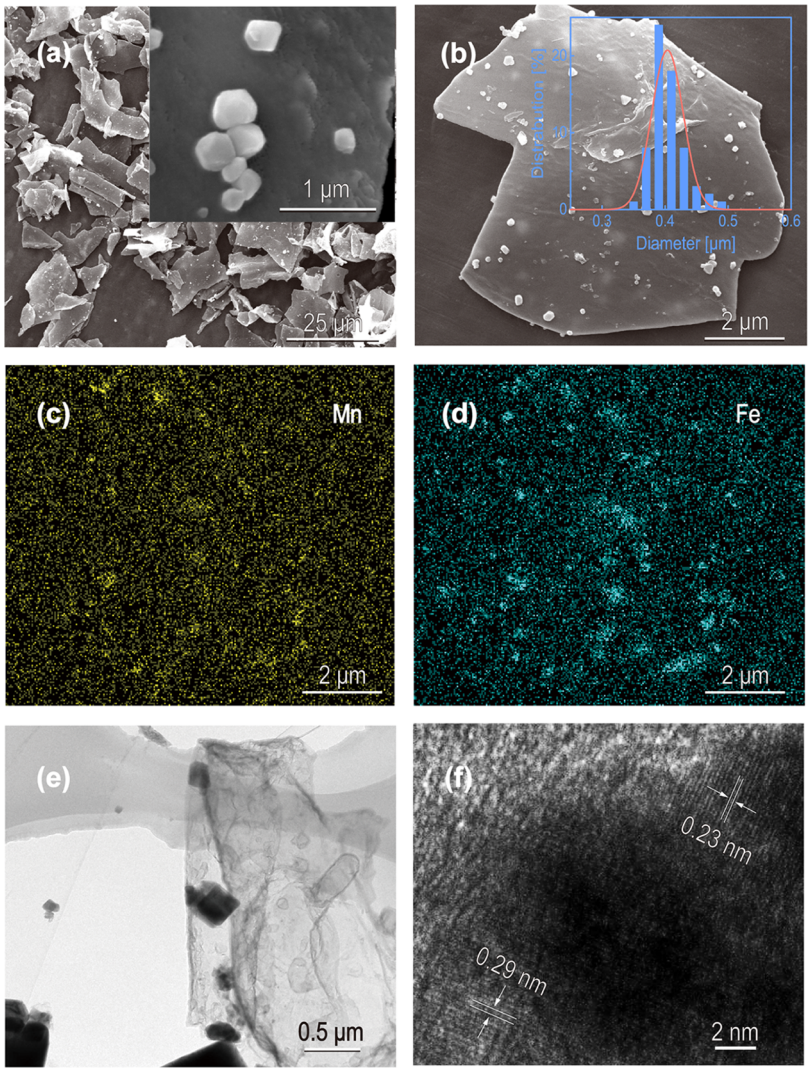

Figure 1. SEM images (a), element micrograph region (b), energy-dispersive system (EDS) mapping patterns of Mn (c), Fe (d), TEM image (e), and HRTEM image (f) of MFSCBB-MCs. The insets (a, b) represent the appearances and the diameter distribution histogram of $MnFe_2O_4$ particles, respectively.

2.2. Batch Experiments. Effects of operational parameters, such as adsorbent dose, pH, temperature, and initial lead concentration on lead adsorption performance of MFSCBB-MCs as well as the adsorption mechanism were investigated. A standard 1000 mg·L^{-1} lead solution was prepared by adding lead nitrate into a volumetric flask and diluting it to obtain the desired concentrations. A predetermined amount of MFSCBB-MCs was dispersed in an aqueous solution of lead under constant shaking using a thermostatic shaker (SYC-C, Shanghai Shengke Instrument Equipment Co., Ltd., China) at 200 rpm. The magnetic separation of MFSCBB-MCs was performed and a 0.2 μm syringe filter was used to filter the solution. The concentration of the remaining lead solution was determined by atomic absorption spectroscopy (WYS2200, AnHui Wanyi Science and Technology Co., Ltd., China). The removal rate, adsorption capacity, adsorption isotherms, and kinetics were determined using various equations (Table S1, Supporting information). The effect of pH on adsorption was investigated over a wide pH range (pH 2−8) through adjustment using HCl and NaOH solution. The effect of ionic strength (KNO_3, Ca $(NO_3)_2$) on adsorption was also evaluated.

2.3. Recyclability Tests. Reusability is an important economic parameter of adsorbents. Adsorption−desorption experiment was carried out to explore the recovery of lead adsorbed to MFSCBB-MCs during the adsorption process. The process was carried out as follows: 0.2 g of MFSCBB-MCs was added to 100 mL of lead-contaminated aqueous solution (10 mg·L^{-1}). After achieving adsorption equilibrium and magnetic separation, the separated adsorbents were mixed with 100 mL of sodium acetate solution (1.0 M). The mixture was oscillated continuously in a shaker incubator at 200 rpm for 12 h at 25 °C. The absorbent was collected, washed with ultrapure water, and dried before use in the next adsorption−desorption cycle. Five cycles were conducted under the same conditions.

3. RESULTS AND DISCUSSION

3.1. Physicochemical Properties of MFSCBB-MCs. A facile and convenient pyrosis method was used to simultaneously complete the biochar transformation and crystallization of metals for a one-step fabrication of magnetic biochar. Surface morphologies and chemical composition of MFSCBB-MCs were explored using scanning electron microscopy (SEM), SEM energy-dispersive X-ray (SEM-EDX), and

https://doi.org/10.1021/acsomega.2c04882
ACS Omega 2022, 7, 42854−42864

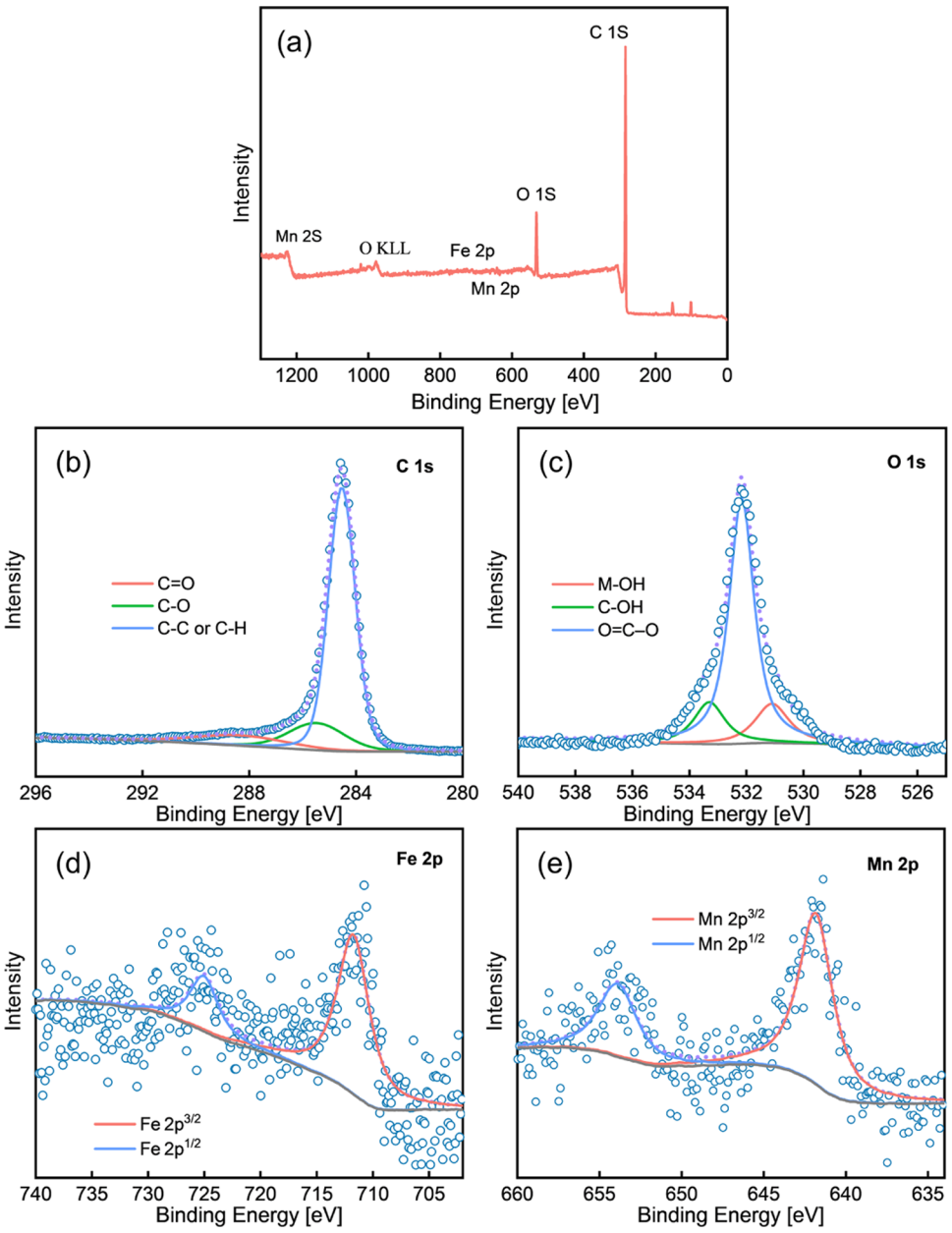

Figure 2. (a) XPS survey spectrum and high-resolution XPS spectra of (b) C 1s, (c) O 1, (d) Fe 2p, and (e) Mn 2p for MFSCBB-MCs.

transmission electron microscopy (TEM) (Figure 1). The SEM investigation revealed that the carbon layer of MFSCBB-MCs was rough, wrinkled, and uneven, with numerous crystal-like tiny particles (Figure 1a,b). Notably, TEM analysis showed consistent results (Figure 1e). *Image J* software (U.S. National Institutes of Health) was used to determine the particle size distribution. The results showed that the particles exhibited a monodispersed polygon shape with an average size of about 400 ± 32 nm. These small particles can provide a lot of extra sites for lead adsorption. Elemental mapping for Figure 1b showed that the particles were mainly composed of Mn, Fe, and O (Figure 1c,d), whereas only C and O were found in the biochar beyond these particles (see Supporting Information Figure S1). The even distribution of C was attributed to bagasse biochar, and O distribution was ascribed to the particles and the oxygen-containing functional group of bagasse biochar. The microstructure of MFSCBB-MCs was further explored by HRTEM and selected area electron diffraction (SAED). HRTEM findings showed relatively clear crystal lattice fringes, indicating the good crystallization property of particles (Figure 1f). The calculated lattice spacing of 0.29 and 0.23 nm was indexed to the (220) and (222) planes of the $MnFe_2O_4$ crystal, respectively. SAED pattern in Figure S2a showed several evident diffraction rings, indicating the formation of $MnFe_2O_4$ crystals. The lattice planes of (111), (220), (311), (400), (440), and (511) were marked and were in accordance with the standard JCPDS card no. 10-0319. The amorphous layer observed around the crystals was attributed to the presence of biochar.[25,26]

The crystallographic structure of MFSCBB-MCs was characterized by X-ray powder diffraction measurement in the range of 2θ (10−80°) (Figure S2a). The diffraction peaks at 2θ = 18.3, 29.8, 35.8, 36.6, 42.8, 52.8, 56.5, and 62.0° accurately matched with the (111), (220), (311), (222), (400), (422), (511), and (440) planes from the JCPDS card (10-0319) for cubic spinel-type $MnFe_2O_4$. Notably, a slight

https://doi.org/10.1021/acsomega.2c04882
ACS Omega 2022, 7, 42854−42864

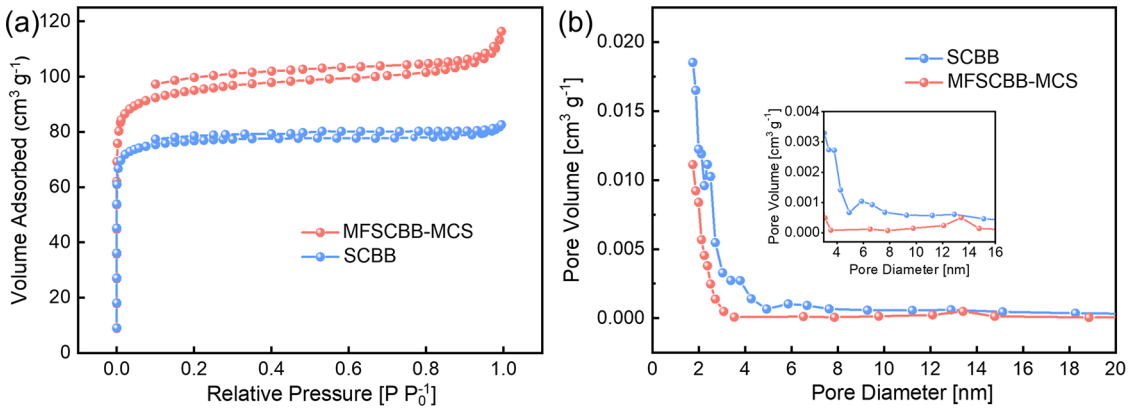

Figure 3. N_2 adsorption and desorption isotherms determined at 76 K (a) and pore size distributions (b) of SCB and MFSCBB-MCs.

broad peak was observed at about 21°. The amorphous component was attributed to the disordered carbon in the sample.[27] This result was compatible with HRTEM and SAED findings, indicating that MFSCBB-MCs were successfully synthesized.

FTIR was performed to explore the surface functional groups of MFSCBB-MCs, and the resultant spectrum is shown in Figure S2b. The broad band observed at about 3440 cm^{-1} was ascribed to the −OH stretching vibration. The absorption bands peaking at 2973, 2919, and 2850 cm^{-1} corresponded to C−H stretching in the aliphatic structures. Peaks at 1635 and 1382 cm^{-1} represented the C═O asymmetric and symmetric stretchings of surface oxygen-containing functional groups. The C−O stretching vibration that occurred at 1078 cm^{-1} was also attributed to oxygen-containing functional groups.[28,29] Two characteristic peaks at 670 and 443 cm^{-1} corresponding to Fe−O and Mn−O vibrations were observed, indicating the presence of $MnFe_2O_4$.[30]

The XPS survey spectrum and high-resolution XPS spectra were used to further explore the chemical composition of MFSCBB-MCs (Figure 2). The findings showed the presence of photoelectron peaks of C 1s, O 1s, Fe 2p, and Mn 2p in MFSCBB-MCs (Figure 2a). The high-resolution C 1s spectrum was deconvolved into three components centered at 288.2 (C═O), 285.4 (C−O), and 284.5 (C−C or C−H) eV. In addition, the O 1s spectrum comprised three components centered at 531.1, 533.3, and 532.6 eV, which were attributed to the hydroxyl bonded to metal (M−OH), O═C−O species, and C−OH, respectively.[31] These findings indicate that MFSCBB-MCs are rich in oxygen-containing functional groups, including hydroxyl groups. The presence of $MnFe_2O_4$ was demonstrated by the simultaneous occurrence of Fe 2p and Mn 2p signals. The Fe 2p signal was represented by three Gaussian functions, which corresponded to different bonding states with binding energy centered at 711.8 (Fe $2p^{3/2}$) and 725.1 (Fe $2p^{1/2}$), respectively. Analysis of the Mn 2p signal revealed two components with binding energy centered at 641.9 (Mn $2p^{3/2}$) and 654.0 (Mn $2p^{1/2}$) eV, respectively.[32,33]

The specific surface area and pore size distributions of SCB and MFSCBB-MCs are presented in Figure 3. The results showed that SCB and MFSCBB-MCs exhibited a typical type I curve with a sharp increase in a 0−0.1 range of relative pressure (Figure 3a). This indicates the predominant microporous characteristics. The surface area of SCB was approximately 373.32 $m^2 \cdot g^{-1}$. The surface area slightly decreased to 305.41 $m^2 \cdot g^{-1}$ after loading $MnFe_2O_4$ to form MFSCBB-MCs. This was attributed to a few adsorption sites on the external surface of SCB, which were occupied by deposited $MnFe_2O_4$ nanoparticles. The findings on the pore size distribution (Figure 3b) showed that SCB and MFSCBB-MCs had microporous (pore size < 2 nm) and mesoporous (2 nm < pore size < 50 nm) structures, respectively. Mesopores with sizes ranging from 3 to 8 nm were blocked and new mesopores with sizes of approximately 13.5 nm occurred during the formation of $MnFe_2O_4$ nanoparticles. The most important micropores (pore size < 2 nm) to the overall pore volumes were preserved. The total pore volume of MFSCBB-MCs (0.10 $cm^3 \cdot g^{-1}$) was therefore not significantly different from that of SCB (0.13 $cm^3 \cdot g^{-1}$). These results indicated that hierarchical porous MFSCBB-MCs were successfully fabricated. This characteristic structural feature of the composite provides more adsorption sites for lead removal.

A vibrating sample magnetometer was used to explore magnetic field-dependent characteristics of MFSCBB-MCs at room temperature. The essential magnetic parameters were obtained from the hysteresis loops presented in Figure 4. The saturation magnetization (M_s) was 4.5 emu·g^{-1}. The remnant magnetization (M_r) and coercivity (H_c) were approximately 0.52 emu·g^{-1} and 97 Oe, respectively. The results showed that MFSCBB-MCs dispersed in an aqueous medium were separated within 5 min after the application of an external magnetic field, exhibiting outstanding magnetic separation

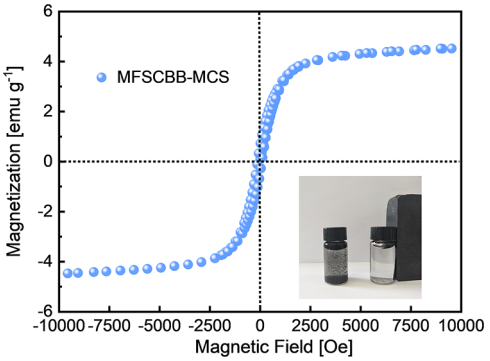

Figure 4. Room-temperature magnetic hysteresis loops of MFSCBB-MCs. The inset figure represents 0.03 mg·mL^{-1} MFSCBB-MCs dispersed in a solution containing 0.03 mg·mL^{-1} Pb, and the behaviors in response to magnetic fields (photograph courtesy of 'Sheng Yu'. Copyright 2022).

https://doi.org/10.1021/acsomega.2c04882
ACS Omega 2022, 7, 42854−42864

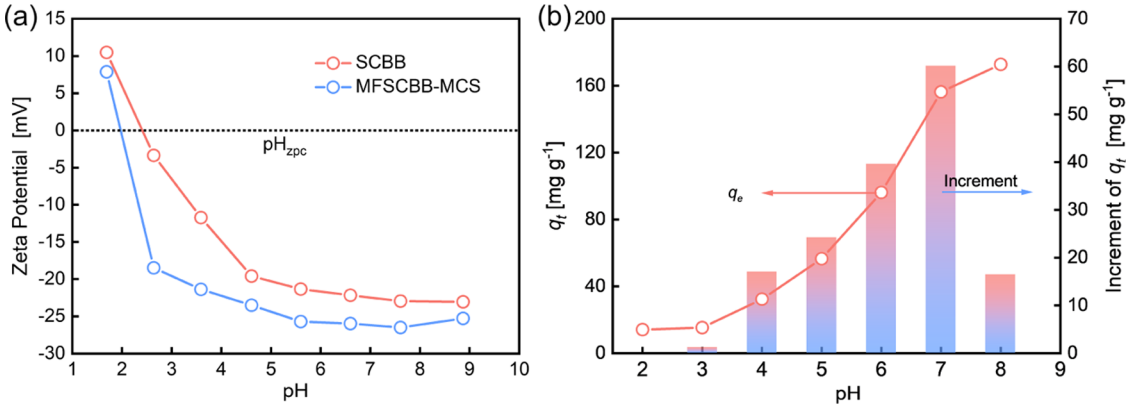

Figure 5. (a) ζ-potential of SCBB and MFSCBB-MCs. (b) Effect of pH on adsorption of lead by MFSCBB-MCs (dosage = 0.1 g·L^{-1}, contact time = 2 h, the initial C_{lead} = 20 mg·L^{-1}).

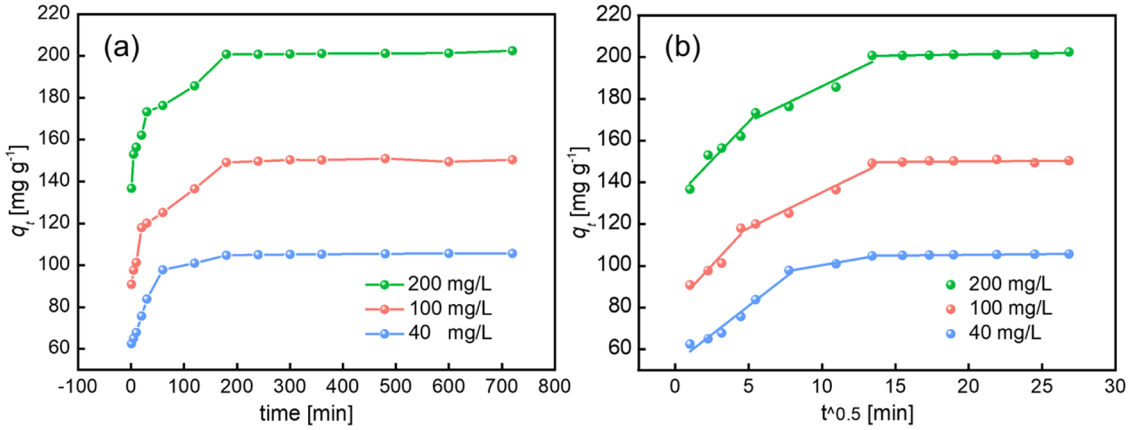

Figure 6. Effect of contact time on lead adsorption capacity (a) and intraparticle diffusion plots for lead adsorption (b) (dosage = 0.1 g·L^{-1}, pH = 6.8).

characteristics. The dispersion became translucent from dark-black color after the completion of the recovery. These findings indicate that MFSCBB-MCs had excellent magnetic properties, which were favorable for adsorption separation and desorption regeneration.

3.2. Effect of Adsorbent Dosage on Adsorption. Adsorbent dosage is a significant parameter as it determines the metal-adsorbent equilibrium within the adsorption system. The effect of biochar dose on lead adsorption for MFSCBB-MCs is shown in Figure S3. The lead removal efficiency increased from 34.1 to 71.8 % as the biochar dose increased, whereas the adsorption efficiency (q_t) decreased from 66.82 to 24.23 mg·g^{-1}. The increase in lead removal percentage can be attributed to the availability of more adsorption sites in the solution. An increase in the biochar dose above a particular dose showed a plateau in the lead removal percentage. This phenomenon can be attributed to competition among the active sites as well as a decrease in the metal ion concentration gradient. Moreover, a reduction in the surface area and an increase in the diffusional path length associated with aggregation/agglomeration of sorbent particles at higher doses can result in a decrease in adsorption capability (q_e). These effects as well as previous findings that additional adsorption sites are available at high pollutant amounts,[34] indicate that the q_t value can be used to approximate the adsorption-saturation capacities under low doses.

3.3. Effect of Initial pH on Adsorption. The pH of the initial solution can affect the ionic form of the contaminant and the adsorbent's functional surface. pH-related protonation or deprotonation of the functional groups can change the adsorbent surface charge distribution. Precipitation of lead hydroxide occurs when the aqueous solution pH reaches 8.0, so the experiment of the influence of pH on lead adsorption performance on MFSCBB-MCs was manifested in the pH range of 2.0−8.0 (Figure 5b). The results showed that the lead removal ability of the prepared magnetic adsorbent was strongly pH-dependent. The adsorption capacity increased significantly by increasing the pH of the solution from 2 to 7, whereas the increase was not significant when the pH was increased from 7 to 8. Accordingly, it can be easily concluded that the optimum pH for lead adsorption is around 7.0. The ζ potentials of the samples (Figure 5a) showed that the pH$_{zpc}$ of MFSCBB-MCs was about 2.0, which was lower than that of SCBB, owing to the incorporation of $MnFe_2O_4$. The oxygen-containing functional groups, derived from both biochar and $MnFe_2O_4$ particles, were continually deprotonated when the pH was increased to 7.0, resulting in a more negatively charged surface. Notably, the predominant lead species at pH ≤ 7.0 was Pb^{2+}.[35] Therefore, an anticipated strong intersection occurred between the negative MFSCBB-MCs surface and the cationic Pb^{2+} species, although particular chemical adsorption cannot be excluded as a significant contributing force in metal ion adsorption.

https://doi.org/10.1021/acsomega.2c04882
ACS Omega 2022, 7, 42854−42864

Table 1. Parameters for the Adsorption of Lead on MFSCBB-MCs Obtained from Different Kinetic Models

kinetic model	parameter	initial conc. ($mg·L^{-1}$)		
		40	100	200
	$q_{e\ exp}$ ($mg·g^{-1}$)	105.65	150.38	202.53
pseudo-first-order	$q_{e\ cal}$ ($mg·g^{-1}$)	42.88	60.89	60.75
	k_1 (h^{-1}) × 10^{-2}	2.12	1.88	1.70
	R^2	0.9727	0.8929	0.8821
pseudo-second-order	$q_{e\ cal}$ ($mg·g^{-1}$)	106.61	148.59	199.20
	k_2 ($g·mg^{-1}\ min^{-1}$) × 10^{-2}	0.94	0.67	0.50
	R^2	0.9979	0.9955	0.9970
Elovich	α ($mg·g^{-1}·min^{-1}$)	320.36	1760.99	115 176.18
	β ($g·mg^{-1}$) × 10^{-1}	1.07	0.90	0.87
	R^2	0.8868	0.9249	0.9507
intraparticle diffusion	K_{id1} ($mg·g^{-1}·min^{-1/2}$)	5.47	7.57	7.348
	C_1 ($mg·g^{-1}$)	53.49	81.39	132.30
	R^2	0.96	0.89	0.93
	K_{id2} ($mg·g^{-1}·min^{-1/2}$)	0.99	3.42	3.40
	C_2 ($mg·g^{-1}$)	90.29	100.96	152.03
	R^2	0.92	0.96	0.89
	K_{id3} ($mg·g^{-1}·min^{-1/2}$)	0.06	0.05	0.10
	C_3 ($mg·g^{-1}$)	104.13	148.98	199.16
	R^2	0.955	0.92	0.89

Table 2. Langmuir and Freundlich Isotherm Parameters for Lead Desorption on MFSCBB-MCs

isotherm model	parameter	temperature (K)		
		298	308	318
	$q_{e\ exp}$ ($mg·g^{-1}$)	150.87	230.07	243.52
Langmuir	q_{max} ($mg·g^{-1}$)	155.21	232.93	240.83
	K_L ($L·mg^{-1}$)	7.00×10^{-2}	8.20×10^{-2}	3.83×10^{-1}
	R^2	0.9935	0.9996	0.9998
	R_L	0.525−0.058	0.529−0.053	0.368−0.011
Freundlich	K_F ($mg^{1-n}·L^n·g^{-1}$)	52.61	102.95	176.78
	n	5.06	6.31	16.84
	R^2	0.8782	0.9123	0.8000

3.4. Adsorption Kinetics. Adsorption kinetics were explored at different initial concentrations of lead(II). The effect of contact time on the adsorption of lead onto MFSCBB-MCs is presented in Figure 6a. Within the first 60 min, lead(II) was quickly adsorbed onto MFSCBB-MCs. The adsorption rate then gradually decreased, whereas the adsorption efficiency increased to >85% and equilibrium was attained within 180 min. Notably, limited additional adsorption was observed after 180 min. Adsorption gradually increased with a further increase in C_0.

Pseudo-first-order, pseudo-second-order, and Elovich models are used to fit the experimental kinetic data to further understand the kinetic mechanism of adsorption. The fitting results, as well as the values of the characteristic parameters, are tabulated in Table 1. The values of k_1 and k_2 for the first-order and second-order kinetic models were obtained from their respective linearized plots as shown in Figure S4. The results of the pseudo-first-order model showed that the value of the calculated q_e was less than that of the experimental q_e, indicating that the pseudo-first-order model did not fit this adsorption kinetic. The high correlation coefficient ($R^2 > 0.99$) based on the pseudo-second-order model offered a better explanation of lead adsorption on MFSCBB-MCs compared with the pseudo-first-ordination model. Furthermore, the calculated q_e values of the pseudo-second-order model were close to the experimental values. These results implied that the rate-limiting step was chemisorption involving valence forces through electron sharing or exchange between the adsorbate and adsorbent.[24] The plot of q_t versus $\ln t$ derived from the Elovich equation, which effectively describes the predominant chemical absorption on highly heterogeneous sorbents, offered an inferior correlation coefficient by linear fitting. However, the significantly higher α value relative to the β value indicated that lead cations were adsorbed on MFSCBB-MCs mainly through the formation of coordination bonds.[36]

To further explore the actual adsorption rate-controlling step, the kinetic adsorption data were fitted using the Weber−Morris model. The fitted results are depicted in Figure 6b and Table 2. Intraparticle diffusion plots showed a multilinear feature, indicating the presence of two or more steps in the sorption process. The intraparticle diffusion rate constant determined from the slope was $K_{id1} > K_{id2} > K_{id3}$. The large slope in the first stage implied that instantaneous adsorption and external diffusion were achieved within a short time. The external surface diffusion slowed down and the adsorption mainly occurred in microscopic pores in the second step, resulting in a sharp decrease in the slope. The slope decreased toward zero thereafter, and the adsorption gradually changed to equilibrium. Notably, linear fitting of the Weber−Morris model exhibited a nonzero intercept, showing that the adsorption process depended on intraparticle diffusion and extra diffusive resistance was involved.[37]

https://doi.org/10.1021/acsomega.2c04882
ACS Omega 2022, 7, 42854−42864

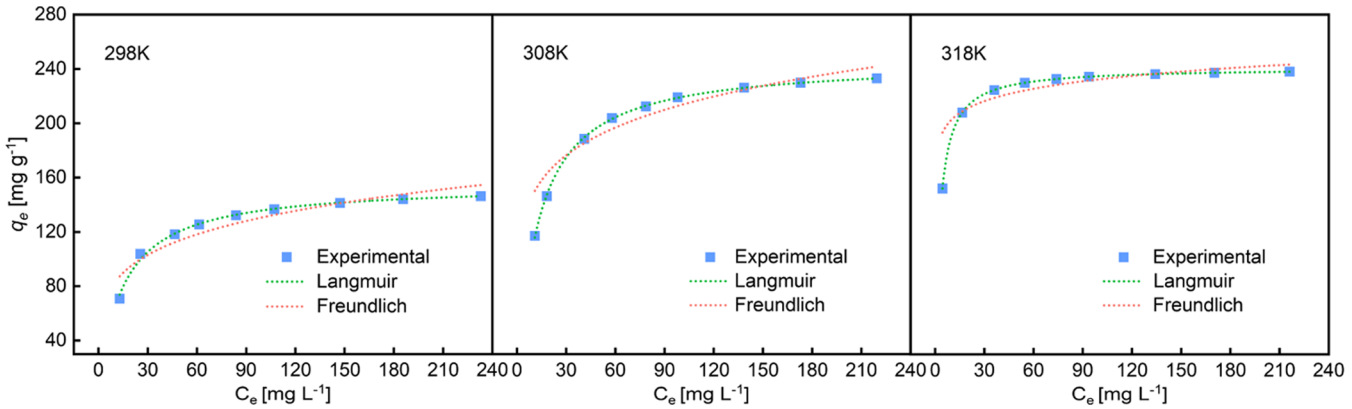

Figure 7. Adsorption isotherm of lead on MFSCBB-MCs at three different temperatures (dosage = 0.1 g·L^{-1}; pH = 6.8; contact time = 3 h).

3.5. Adsorption Isotherms. Adsorption isotherms at three different temperatures (298, 308, and 318 K) were obtained by changing the lead concentration from 0 to 240 mg. The Langmuir and Freundlich models were then used to fit equilibrium data. Adsorption isotherms of lead on MFSCBB-MCs under the three different temperatures, including the fitting of the experimental data, are shown in Figure 7. The fitted values of the characteristic parameters and the coefficients (R^2) are presented in Table 3. The Langmuir model showed a higher correlation of the experimental isothermal data concerning the high determination coefficients compared with the Freundlich model. This indicates that adsorption was a uniform and monolayer coverage process.[38] The dimensionless separation factor (R_L) for all of the adsorption processes in the Langmuir model was in the range of 0−1, indicating that the adsorption process for this model was favorable.[39] The theoretical maximum adsorption capacity (q_{max}) at room temperature was calculated to be 155.21 mg·g^{-1}. The results showed that MFSCBB-MCs exhibited a high lead adsorption capacity when compared to the q_{max} of other modified bagasse adsorbents previously proposed for lead removal, as shown in Table S2.

Table 3. Thermodynamic Parameters of Lead Adsorption over the MFSCBB-MCs Adsorbent at Three Temperatures

T (K)	$\Delta G°$ (kJ·mol^{-1})	$\Delta H°$ (kJ·mol^{-1})	$\Delta S°$ (J·mol^{-1}·K^{-1})
308	−4.07	74.08	261.41
323	−5.90		
338	−9.33		

3.6. Adsorption Thermodynamics. Thermodynamic parameters were calculated to further investigate if lead adsorption on MFSCBB-MCs occurs spontaneously. The parameters including ΔG (Gibbs free energy), ΔH (enthalpy), and ΔS (entropy) were calculated using the following equations

$$\Delta G = -RT \ln K_c \quad (1)$$

$$\ln K_c = -\Delta H/RT + \Delta S/R \quad (2)$$

where R is the general gas constant (8.314 J·mol^{-1}·K^{-1}), T is the absolute temperature (K), and K_c is the thermodynamic equilibrium constant (L·g^{-1}). Based on the experimental data provided in Figure 7, a linear plot of $\ln K_c$ versus $1/T$ was obtained. ΔH and ΔS of the adsorption process were calculated according to eq 2, using the slope and intercept of the plot, respectively. The difference between the adsorption enthalpy and adsorption entropy derived from eq 1, multiplied by the temperature, gives Gibbs free energy. The calculated values of ΔG, ΔH, and ΔS are presented in Table 3. The positive value of ΔH indicated that the lead adsorption process was an endothermic process, and the positive value of ΔS implied that the adsorbent/liquid interface became more disordered. The results showed that all of the values of ΔG were negative, and their absolute values increased as the temperature increased, indicating spontaneous lead adsorption upon MFSCBB-MCs at the three temperatures.[40]

3.7. Sorption Mechanism. The hierarchically porous MFSCBB-MCs with a large specific surface area were beneficial for the capture of lead(II) by physical adsorption. Meanwhile, the surface electronegativity of MFSCBB-MCs caused electrostatic attraction as well as electrostatic surface complexation with cationic lead(II) species. According to the kinetic study, chemisorption was more important during lead(II) adsorption on MFSCBB-MCs. To further investigate the removal mechanism of lead(II) by MFSCBB-MCs, XPS analysis on the Pb-MFSCBB-MCs sample (after the sorption of Pb^{2+}) was performed (Figure S5). The significant peak corresponding to Pb 4f was observed on the MFSCBB-MCs surface in Figure S5a, indicating the successful adsorption of Pb^{2+} by MFSCBB-MCs. The Pb 4f spectrum comprised two components centered at 139.0 and 143.9 eV, which were assigned to Pb $4f^{7/2}$ and Pb $4f^{5/2}$, respectively (Figure S5b). The energy separation of 4.9 eV between the Pb 4f5/2 and 4f7/2 confirmed the coordination interaction between Pb^{2+} and MFSCBB-MCs.[41] The Pb $4f^{7/2}$ peak, which shifted to lower binding energy than that of lead nitrate (139.5 eV), was ascribed to the binding (Pb−O) formed with the hydroxyl groups, while the Pb 4f5/2 peak was attributed to the binding (Pb−OOC) formed with the carboxyl groups on $MnFe_2O_4$ or the biochar surface of MFSCBB-MCs. The high-resolution Fe 2p, Mn 2p, and O 1s spectra also corroborated it. After lead(II) adsorption, Fe 2p (Figure S5d) and Mn 2p (Figure S5e) showed a slight shift in the binding energy. This may be explained by the transformation from Fe/Mn−OH to $(Fe/Mn-O)_2Pb$ or Fe/Mn−COOH to $(Fe/Mn-COO)_2Pb$.[42] Three components of the O 1s spectrum located at 531.1, 533.3, and 532.6 eV (Figure 2c) shifted to 530.4, 533.5, and 532.1 eV (Figure S5c), which were attributed to the formation of Mn/Fe−O−Pb, C−O−Pb, and Mn/Fe−COO−Pb or COO−Pb on the surface of MFSCBB-MCs.[43] These results suggest that the oxygen-containing functional groups on

https://doi.org/10.1021/acsomega.2c04882
ACS Omega 2022, 7, 42854−42864

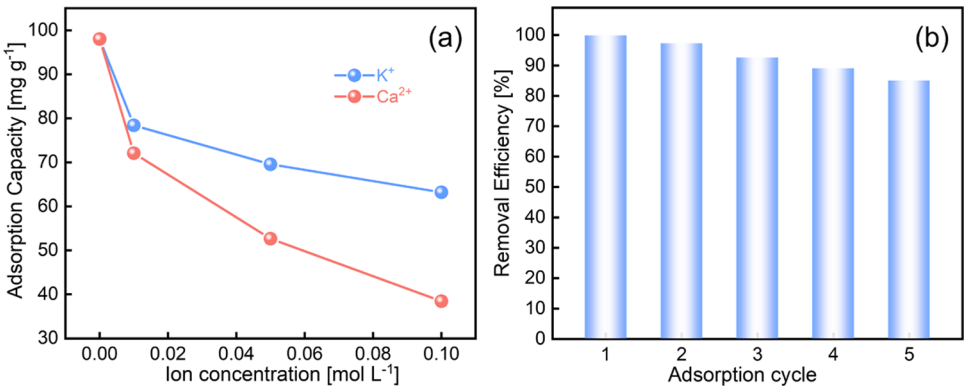

Figure 8. (a) Effect of various co-ions on lead removal by MFSCBB-MCs. (b) Reusability of MFSCBB-MCs during five cycles.

MFSCBB-MCs are crucial for the high lead(II) adsorption ability. The lead(II) adsorption process on MFSCBB-MCs involves physical adsorption, electrostatic attraction, and complexation.

3.8. Effect of Coexisting Ions. The results from the ζ-potential experiments showed that the introduction of $MnFe_2O_4$ resulted in a highly negatively charged surface of the composites (MFSCBB-MCs) at a pH ≥3. Previous studies reported that the binding of cations to a negatively charged surface neutralizes the surface charge.[44] Gradient concentrations of KNO_3 and $Ca(NO_3)_2$ ranging from 0.02 to 0.1 M were used to explore the effect of coexisting cation ions, K^+ and Ca^{2+}, on lead adsorption. The cations in solution increase the electrostatic repulsion between cations and lead or can compete with lead for the active sorption sites. Lead adsorption capacity significantly decreased with an increase in ionic strength (Figure 8a). Ca^{2+} showed a significant effect on lead adsorption compared with the effect of K^+. This can be partially attributed to the higher positive charge of Ca^{2+}. Thus, they effectively shield more negative charges on MFSCBB-MCs as well as occupy more active sites.

3.9. Regeneration and Reusability. The capacity of the adsorbent to regenerate for practical application is critical for enhancing the cost efficiency of the adsorption process. In the present study, lead desorption was performed by dispersing exhausted MFSCBB-MCs into 1 M CH_3COONa aqueous solution at room temperature. The regenerated adsorbent was then used to remove lead from water under the same conditions. The results showed that the lead removal percentage was maintained above 85% after five sorption−desorption cycles (Figure 8b). This indicates that MFSCBB-MCs can be repeatedly and effectively used as an adsorbent for lead removal, thus reducing the cost of the process. Notably, CH_3COONa treatment promotes the desorption of adsorbed lead from MFSCBB-MCs.

4. CONCLUSIONS

In the present study, $MnFe_2O_4$/SCB biochar magnetic composites (MFSCBB-MCs) were successfully prepared through a one-step pyrolysis method and used as a recoverable absorbent for lead removal from water, with the benefits of bagasse resource utilization and facile separation. The incorporation of $MnFe_2O_4$ resulted in a more negatively charged surface, which was more effective for cation capture. Adsorption kinetics and adsorption thermodynamics studies indicated that lead adsorption on MFSCBB-MCs was spontaneous chemisorption and endothermic in nature. The sorption of lead on MFSCBB-MCs included physical adsorption, electrostatic attraction, and complexation, and they showed higher lead adsorption capability compared with previously reported bagasse adsorbents for lead removal. The exhausted adsorbent was regenerated and recycled through chemical desorption with the aid of magnetic $MnFe_2O_4$ using a magnetic field, implying that MFSCBB-MCs have a high potential for environmental application and are relatively affordable.

■ ASSOCIATED CONTENT

Supporting Information

The Supporting Information is available free of charge at https://pubs.acs.org/doi/10.1021/acsomega.2c04882.

Materials used in this study and characterization of MFSCBB-MCs. Equations and parameters of q_t, removal rate, kinetic and isotherm models, the carbon and oxygen element mapping, elemental analysis, FTIR spectrum, SAED pattern, XRD pattern of MFSCBB-MCs, effect of adsorbent dose and linear fits of pseudo-first-order, pseudo-second-order, and Elovich equations for Pb adsorption on MFSCBB-MCs. Adsorption capacities of different bagasse sorbents for lead (PDF)

■ AUTHOR INFORMATION

Corresponding Author

Hejun Gao − *Chemical Synthesis and Pollution Control Key Laboratory of Sichuan Province, College of Chemistry and Chemical Engineering, China West Normal University, Nanchong 637000, China*; Email: hejun_gao@126.com

Authors

Jinming Chang − *Chemical Synthesis and Pollution Control Key Laboratory of Sichuan Province, College of Chemistry and Chemical Engineering, China West Normal University, Nanchong 637000, China*; orcid.org/0000-0001-5069-2824

Sheng Yu − *Chemical Synthesis and Pollution Control Key Laboratory of Sichuan Province, College of Chemistry and Chemical Engineering, China West Normal University, Nanchong 637000, China*

Yunwen Liao − *Chemical Synthesis and Pollution Control Key Laboratory of Sichuan Province, College of Chemistry and Chemical Engineering, China West Normal University, Nanchong 637000, China*

Xiaoyu Guan − *Shaanxi Collaborative Innovation Center of Industrial Auxiliary Chemistry & Technology, Shaanxi*

https://doi.org/10.1021/acsomega.2c04882
ACS Omega 2022, 7, 42854−42864

University of Science & Technology, Xian 710021, China; orcid.org/0000-0001-5791-731X

Yulong Li − *Key Laboratory of Green Chemistry of Sichuan Institutes of Higher Education, Sichuan University of Science & Engineering, Zigong 643000, China*

Complete contact information is available at: https://pubs.acs.org/10.1021/acsomega.2c04882

Author Contributions

The manuscript was written through contributions of all authors. All authors have given approval to the final version of the manuscript.

Notes

The authors declare no competing financial interest.

■ ACKNOWLEDGMENTS

The authors gratefully acknowledge the financial support from the Science and Technology Planning Project of Sichuan Province (No. 2022NSFSC0350), the Opening Project of Key Laboratory of Green Chemistry of Sichuan Institutes of Higher Education (No. LZJ1902), the Open Project of Shaanxi Collaborative Innovation Center of Industrial Auxiliary Chemistry & Technology (No. XTKF-2020-02), the Opening Project of Key Laboratory of Leather Chemistry and Engineering (Sichuan University, 2020), the Ministry of Education, the Ph.D. Start-up Fund (No. 18Q025), and the Basic Scientific Research Operating Expense Project (No. 416981) of China West Normal University.

■ REFERENCES

(1) Li, H.; Dong, X.; da Silva, E. B.; de Oliveira, L. M.; Chen, Y.; Ma, L. Q. Mechanisms of metal sorption by biochars: biochar characteristics and modifications. *Chemosphere* **2017**, *178*, 466−478.

(2) Verma, M.; Lee, I.; Sharma, S.; Kumar, R.; Kumar, V.; Kim, H. Simultaneous removal of heavy metals and ciprofloxacin micropollutants from wastewater using ethylenediaminetetraacetic acid-functionalized beta-cyclodextrin-chitosan adsorbent. *ACS Omega* **2021**, *6*, 34624−34634.

(3) Liu, Z.; Gao, Z.; Xu, L.; Hu, F. Polypyrrole modified magnetic reduced graphene oxide composites: synthesis, characterization and application for selective lead adsorption. *RSC Adv.* **2020**, *10*, 17524−17533.

(4) Ghorbani, M.; Seyedin, O.; Aghamohammadhassan, M. Adsorptive removal of lead (II) ion from water and wastewater media using carbon-based nanomaterials as unique sorbents: A review. *J. Environ. Manage.* **2020**, *254*, No. 109814.

(5) Manfrin, J.; Gonçalves, A. C., Jr; Schwantes, D.; Conradi, E., Jr; Zimmermann, J.; Ziemer, G. L. Development of biochar and activated carbon from cigarettes wastes and their applications in Pb^{2+} adsorption. *J. Environ. Chem. Eng.* **2021**, *9*, No. 104980.

(6) Zhang, Y.; Alessi, D. S.; Chen, N.; Luo, M.; Hao, W.; Alam, M. S.; Flynn, S. L.; Kenney, J. P. L.; Konhauser, K. O.; Ok, Y. S.; Al-Tabbaa, A. Lead (Pb) sorption to hydrophobic and hydrophilic zeolites in the presence and absence of MTBE. *J. Hazard. Mater.* **2021**, *420*, No. 126528.

(7) Ebadollahzadeh, H.; Zabihi, M. Competitive adsorption of methylene blue and Pb (II) ions on the nano-magnetic activated carbon and alumina. *Mater. Chem. Phys.* **2020**, *248*, No. 122893.

(8) Ayalew, A. A. A critical review on clay-based nanocomposite particles for application of wastewater treatment. *Water Sci. Technol.* **2022**, *85*, 3002−3022.

(9) Ai, S.; Huang, Y.; Huang, C.; Yu, W.; Mao, Z. Lead ion adsorption on functionalized sugarcane bagasse prepared by concerted oxidation and deprotonation. *Environ. Sci. Pollut. Res.* **2021**, *28*, 2728−2740.

(10) Halysh, V.; Sevastyanova, O.; Pikus, S.; Dobele, G.; Pasalskiy, B.; Gun'ko, V. M.; Kartel, M. Sugarcane bagasse and straw as low-cost lignocellulosic sorbents for the removal of dyes and metal ions from water. *Cellulose* **2020**, *27*, 8181−8197.

(11) Aruna; Bagotia, N.; Sharma, A. K.; Kumar, S. A review on modified sugarcane bagasse biosorbent for removal of dyes. *Chemosphere* **2020**, *268*, No. 129309.

(12) Zheng, X.; Zhou, Y.; Liu, X.; Fu, X.; Peng, H.; Lv, S. Enhanced adsorption capacity of MgO/N-doped active carbon derived from sugarcane bagasse. *Bioresour. Technol.* **2020**, *297*, No. 122413.

(13) Prasannamedha, G.; Kumar, P. S.; Mehala, R.; Sharumitha, T.; Surendhar, D. Enhanced adsorptive removal of sulfamethoxazole from water using biochar derived from hydrothermal carbonization of sugarcane bagasse. *J. Hazard. Mater.* **2021**, *407*, No. 124825.

(14) Prasannamedha, G.; Senthil Kumar, P.; Shankar, V. Facile route for synthesis of $Fe_0/Fe_3C/\Gamma\text{-}Fe_2O_3$ carbon composite using hydrothermal carbonization of sugarcane bagasse and its use as effective adsorbent for sulfamethoxazole removal. *Chemosphere* **2022**, *289*, No. 133214.

(15) El-Banna, M. F.; Mosa, A.; Gao, B.; Yin, X.; Ahmad, Z.; Wang, H. Sorption of lead ions onto oxidized bagasse-biochar mitigates Pb-induced oxidative stress on hydroponically grown chicory: Experimental observations and mechanisms. *Chemosphere* **2018**, *208*, 887−898.

(16) Doumer, M. E.; Rigol, A.; Vidal, M.; Mangrich, A. Removal of Cd, Cu, Pb, and Zn from aqueous solutions by biochars. *Environ. Sci. Pollut. Res.* **2016**, *23*, 2684−2692.

(17) Dong, X.; He, L.; Hu, H.; Liu, N.; Gao, S.; Piao, Y. Removal of 17β-estradiol by using highly adsorptive magnetic biochar nanoparticles from aqueous solution. *Chem. Eng. J.* **2018**, *352*, 371−379.

(18) Yi, Y.; Tu, G.; Zhao, D.; Tsang, P. E.; Fang, Z. Key role of FeO in the reduction of Cr (VI) by magnetic biochar synthesised using steel pickling waste liquor and sugarcane bagasse. *J. Cleaner Prod.* **2020**, *245*, No. 118886.

(19) Mahawong, S.; Dechtrirat, D.; Watcharin, W.; Wattanasin, P.; Muensit, N.; Chuenchom, L. Mesoporous magnetic carbon adsorbents prepared from sugarcane bagasse and Fe^{2+} and Fe^{3+}*via* simultaneous magnetization and activation for tetracycline adsorption. *Sci. Adv. Mater.* **2020**, *12*, 161−172.

(20) Buthiyappan, A.; Gopalan, J.; Raman, A. A. A. Synthesis of iron oxides impregnated green adsorbent from sugarcane bagasse: characterization and evaluation of adsorption efficiency. *J. Environ. Manage.* **2019**, *249*, No. 109323.

(21) Karunanayake, A. G.; Todd, O. A.; Crowley, M.; Ricchetti, L.; Pittman, C. U., Jr; Anderson, R.; Mohan, D.; Mlsna, T. Lead and cadmium remediation using magnetized and nonmagnetized biochar from Douglas fir. *Chem. Eng. J.* **2018**, *331*, 480−491.

(22) Zhao, Y.; Zhang, R.; Liu, H.; Li, M.; Chen, T.; Chen, D.; Zou, X.; Frost, R. L. Green preparation of magnetic biochar for the effective accumulation of Pb (II): Performance and mechanism. *Chem. Eng. J.* **2019**, *375*, No. 122011.

(23) Suwunwong, T.; Danwittayakul, P.; Thanomsilp, C.; Siriwat, P.; Chantrapromma, S.; Phoungthong, K. The removal of Pb^{2+} ion by $MnFe_2O_4$/waste tea leaves biochar and mechanism of adsorption. *Mater. Res. Express* **2021**, *8*, No. 015505.

(24) Zhang, L.; Guo, J.; Huang, X.; Wang, W.; Sun, P.; Li, Y.; Han, J. Functionalized biochar-supported magnetic $MnFe_2O_4$ nanocomposite for the removal of Pb (II) and Cd (II). *RSC Adv.* **2019**, *9*, 365−376.

(25) Fu, H.; Ma, S.; Zhao, P.; Xu, S.; Zhan, S. Activation of peroxymonosulfate by graphitized hierarchical porous biochar and $MnFe_2O_4$ magnetic nanoarchitecture for organic pollutants degradation: Structure dependence and mechanism. *Chem. Eng. J.* **2019**, *360*, 157−170.

(26) Yin, P.; Zhang, L.; Sun, P.; Wang, J.; Feng, X.; Zhang, Y.; Dai, J.; Tang, Y. Apium-derived biochar loaded with $MnFe_2O_4$@C for excellent low frequency electromagnetic wave absorption. *Ceram. Int.* **2020**, *46*, 13641−13650.

(27) Ahmed, W.; Mehmood, S.; Núñez-Delgado, A.; Ali, S.; Qaswar, M.; Khan, Z. H.; Ying, H.; Chen, D.-Y. Utilization of *Citrullus lanatus*

L. seeds to synthesize a novel $MnFe_2O_4$-biochar adsorbent for the removal of U (VI) from wastewater: Insights and comparison between modified and raw biochar. *Sci. Total Environ.* **2021**, *771*, No. 144955.
(28) Noreen, S.; Bhatti, H. N.; Iqbal, M.; Hussain, F.; Sarim, F. M. Chitosan, starch, polyaniline and polypyrrole biocomposite with sugarcane bagasse for the efficient removal of Acid Black dye. *Int. J. Biol. Macromol.* **2020**, *147*, 439−452.
(29) Demiral, H.; Güngör, C. Adsorption of copper (II) from aqueous solutions on activated carbon prepared from grape bagasse. *J. Cleaner Prod.* **2016**, *124*, 103−113.
(30) Jin, C.; Teng, G.; Gu, Y.; Cheng, H.; Fu, S.; Zhang, C.; Ma, W. Functionalized hollow $MnFe_2O_4$ nanospheres: design, applications and mechanism for efficient adsorption of heavy metal ions. *New J. Chem.* **2019**, *43*, 5879−5889.
(31) Guo, J.; Yan, C.; Luo, Z.; Fang, H.; Hu, S.; Cao, Y. Synthesis of a novel ternary HA/Fe-Mn oxides-loaded biochar composite and its application in Cadmium (II) and Arsenic (V) adsorption. *J. Environ. Sci.* **2019**, *85*, 168−176.
(32) Peng, X.; Gao, F.; Zhao, J.; Li, J.; Qu, J.; Fan, H. Self-assembly of a graphene oxide/$MnFe_2O_4$ motor by coupling shear force with capillarity for removal of toxic heavy metals. *J. Mater. Chem. A* **2018**, *6*, 20861−20868.
(33) Ma, Q.; Zhang, H.; Zhang, X.; Li, B.; Guo, R.; Cheng, Q.; Cheng, X. Synthesis of magnetic CuO/$MnFe_2O_4$ nanocompisite and its high activity for degradation of levofloxacin by activation of persulfate. *Chem. Eng. J.* **2019**, *360*, 848−860.
(34) Gao, H.; Zhao, S.; Cheng, X.; Wang, X.; Zheng, L. Removal of anionic azo dyes from aqueous solution using magnetic polymer multi-wall carbon nanotube nanocomposite as adsorbent. *Chem. Eng. J.* **2013**, *223*, 84−90.
(35) Gao, H.; Du, J.; Liao, Y. Removal of chromium (VI) and orange II from aqueous solution using magnetic polyetherimide/sugarcane bagasse. *Cellulose* **2019**, *26*, 3285−3297.
(36) Wang, Q.; Wang, B.; Lee, X.; Lehmann, J.; Gao, B. Sorption and desorption of Pb (II) to biochar as affected by oxidation and pH. *Sci. Total Environ.* **2018**, *634*, 188−194.
(37) Lawal Usman, U.; Kumar Allam, B.; Bahadur Singh, N.; Banerjee, S. Adsorptive removal of Cr (VI) from wastewater by hexagonal boron nitride-magnetite nanocomposites: Kinetics, mechanism and LCA analysis. *J. Mol. Liq.* **2022**, *354*, No. 118833.
(38) Wu, P.; He, Y.; Lu, S.; Wang, S.; Yi, J.; He, Y.; Zhang, J.; Xiang, S.; Ding, P.; Kai, T.; Pan, H. A regenerable ion-imprinted magnetic biocomposite for selective adsorption and detection of Pb^{2+} in aqueous solution. *J. Hazard. Mater.* **2021**, *408*, No. 124410.
(39) Naushad, M.; Ahamad, T.; Al-Sheetan, K. M. Development of a polymeric nanocomposite as a high performance adsorbent for Pb (II) removal from water medium: Equilibrium, kinetic and antimicrobial activity. *J. Hazard. Mater.* **2021**, *407*, No. 124816.
(40) Li, C.; Wang, H.; Zhang, Y. Pb (II) removal from aqueous solution by cold KOH activated biochar of camphor leaves: isotherms, kinetics and thermodynamics. *Desalin. Water Treat.* **2019**, *161*, 327−336.
(41) Abdel-Magied, A. F.; Abdelhamid, H.; Ashour, R.; Fu, L.; Dowaidar, M.; Xia, W.; Forsberg, K. Magnetic metal-organic frameworks for efficient removal of Cadmium (II), and Lead (II) from aqueous solution. *J. Environ. Chem. Eng.* **2022**, *10*, No. 107467.
(42) Ren, Y.; Li, N.; Feng, J.; Luan, T.; Wen, Q.; Li, Z.; Zhang, M. Adsorption of Pb (II) and Cu (II) from aqueous solution on magnetic porous ferrospinel $MnFe_2O_4$. *J. Colloid Interface Sci.* **2012**, *367*, 415−421.
(43) Chen, Y.; Xu, F.; Li, H.; Li, Y.; Liu, Y.; Chen, Y.; Li, M.; Li, L.; Jiang, H.; Chen, L. Simple hydrothermal synthesis of magnetic $MnFe_2O_4$-sludge biochar composites for removal of aqueous Pb^{2+}. *J. Anal. Appl. Pyrolysis* **2021**, *156*, No. 105173.
(44) Song, G.; Shi, Y.; Wang, H.; Li, A.; Li, W.; Sun, Y.; Ding, G. Effective sorptive removal of five cationic dyes from aqueous solutions by using magnetic multi-walled carbon nanotubes. *Water Sci. Technol.* **2022**, *85*, 1999−2014.

https://doi.org/10.1021/acsomega.2c04882
ACS Omega 2022, 7, 42854−42864